

Sn₂Pd: a possible superconducting material with topological surface states

M. M. Sharma^{1,2}, V.P.S. Awana^{1,2}

¹*National Physical Laboratory (CSIR), Dr. K. S. Krishnan Road, New Delhi 110012, India.*

²*Academy of Scientific and Innovative Research, Ghaziabad, U.P. 201002, India.*

Abstract:

In this article, we report the detailed magneto transport measurements of topological semimetal (TSM) candidate, Sn₂Pd. Single crystal of Sn₂Pd is synthesized through self-flux method. Phase purity and crystalline morphology are confirmed through powder X ray diffraction (PXRD) pattern and field emission scanning electron microscopy (FESEM) image. Signatures of superconducting transition are seen in both transport and magneto transport measurements, which are further supported by the AC magnetization studies. Sn₂Pd is found to show superconductivity onset at below 2.8K, but not the zero resistivity down to 2K. Although, isothermal magneto resistivity measurements below superconducting onset (2.8K) clearly exhibited superconductor like behavior, but is not observed in heat capacity measurements, indicating the same to be of weak nature. Magneto transport measurements performed in normal state of Sn₂Pd show the presence of weak antilocalization (WAL) effect, which is confirmed by modelling of low field magneto-conductivity (MC) through Hikami Larkin Nagaoka (HLN) formalism. Here, it is worth mentioning that the present article is the first report on magneto transport measurements of Sn₂Pd, which show the same to be a topological material with weak superconducting phase below around 2.8K.

Keywords: Topological semimetal, superconductivity, weak antilocalization, magneto conductivity, Hikami Larkin Nagaoka model.

PACS: 74.70.Dd, 74.62.Fj, 74.25.F-

*Corresponding Author

Dr. V. P. S. Awana: E-mail: awana@nplindia.org

Ph. +91-11-45609357, Fax-+91-11-45609310

Homepage: awanavps.webs.com

Introduction:

In recent years, the materials with exotic topological phases such as topological insulators (TIs), topological semimetals (TSMs) and topological superconductors (TSCs) have generated a significant interest of condensed matter scientists [1-3]. These topological materials contain exotic topological surface states (TSS), which allows electrical current to

flow without any dissipation [1,2]. TSCs contain a full superconducting gap in bulk states along with topological surface states at the boundary, which are supposed to hosts Majorana fermions [3]. Till now, a lot of efforts have been made to fabricate TSCs, which include heterostructures of conventional superconductor and TI material or high spin orbit coupling (SOC) semiconducting materials [4-6]. Apart from the heterostructures, some of the doped TIs with formula $A_x\text{Bi}_2(\text{Te/Se})_3$ ($A=\text{Cu, Nb, Sr, Tl, Pd}$) [7-11] are found to show topological superconductivity. In regards of topological superconductivity, TSMs are extensively studied due to their high carrier density and intrinsic topological properties [12]. TSMs are interesting materials as the bulk states of these materials show topological non-trivial structure, which is only possible for surface states in case of TIs [2,12,13]. In TSMs, the valence and conduction bands are supposed to show band degeneracy at high symmetry points or lines in Brillouin zone [14] and are linearly dispersed [15]. Linear dispersion of bands in TSMs leads to occurrence of linear magnetoresistance (LMR) in magneto transport measurements [16-18]. TSMs possess high carrier density, which makes them as a prominent candidate to observe superconductivity with topological non-trivial band structure [12].

TSMs having the general formula $X_2\text{Pd}$ ($X=\text{Bi, Pb, Sb}$) are reported to have topological non-trivial band structure along with bulk superconductivity [19-29]. $\beta\text{-Bi}_2\text{Pd}$ is extensively studied for its topological and superconducting properties [19-21]. Monolayer of $\beta\text{-Bi}_2\text{Pd}$ shows evidence of existence of p wave superconductivity, and also the possible signatures of Majorana zero modes [30,31]. The other members of this family viz. Pb_2Pd and Sb_2Pd are lesser studied [22-29]. Sb_2Pd is superconducting below 1.35K with topological non-trivial band structure [22-26]. Another compound Pb_2Pd is also superconducting and the theoretical calculations show the same to be a topological material [27-29]. Simultaneous existence of superconductivity with topological non-trivial band structure makes this family of compounds interesting. Sn_2Pd also belongs to this family of materials, and remained unexplored in context of topological properties. This is despite an early report based on theoretical studies of band structure of Sn_2Pd showing the same to be a TSM [14]. Magneto-transport properties of Sn_2Pd remained unexplored till date as the one and only report available is on the R-T measurements of the same [32]. Lack of experimental studies on Sn_2Pd , motivates us to study its magneto transport and magnetic properties in order to probe possible superconductivity in this TSM.

This article reports the aspects of superconductivity and topological properties of Sn_2Pd single crystal. Single crystal of Sn_2Pd is synthesized through a self-flux method using solid state reaction route. Glimpses of superconductivity are observed in both transport and magnetic

measurements. Interestingly, synthesized Sn₂Pd single crystal is observed to show non saturating LMR, signifying the possible existence of TSS in the studied system. Low field MC data is further analysed using HLN model, which confirmed the presence of WAL effect and shows that the conduction is dominated by TSS at low temperatures.

Experimental:

Sn₂Pd single crystal is grown by using a simple self-flux method. Sn and Pd were taken in stoichiometric ratio (2:1) and grounded in Argon atmosphere inside MBraun made Glove Box. The obtained homogenous powder was then palletized and vacuum encapsulated in quartz ampoule. The sample is then heated to 950°C for 24 hours and then slowly cooled to 580°C at a rate of 2°C/h. The sample was kept at this temperature for 48 hours and then quenched in ice water. The obtained crystal was silvery shiny. The schematic of heat treatment is shown in Fig. 1(a). Rigaku mini flex II table top XRD equipped with Cu-K_α radiation is used to record PXRD pattern. Surface morphology and elemental composition were analysed using MIRA II LMH TESCAN made FESEM equipped Energy Dispersive X-Ray (EDX) detector. Transport, magnetic and thermal measurements were performed using Quantum Design Physical Property Measurement System (QD-PPMS) equipped with ±14T magnet. Full Prof software was used for Rietveld refinement of PXRD data and VESTA software was used to draw the unit cell of synthesized Sn₂Pd single crystal.

Results & Discussion:

Fig. 1(b) depicts Rietveld refined PXRD pattern of synthesized Sn₂Pd single crystal. Rietveld refinement is performed using the parameters of a tetragonal unit cell with I 41/a c d space group symmetry. The PXRD data is found to be well fitted with the applied fitting protocols and the parameter of goodness of fit i.e., χ^2 is found to be 2.20, which is in an acceptable range. All peaks of PXRD pattern are found to be fitted with applied space group symmetry and the parameters of tetragonal phase, and are indexed with their respective planes. The fitted PXRD pattern shows that the sample is phase pure and no secondary phase is present in the system. Also, peaks for individual elemental impurity are not detected in PXRD pattern, which shows that no element remained unreacted. The obtained lattice parameters from Rietveld refinement are $a=b=6.492(4)\text{\AA}$ & $c=24.363(2)\text{\AA}$, $\alpha=\beta=\gamma=90^\circ$. The unit cell parameters along with the fitting parameters are given in table-1. The crystallographic information file (CIF) generated from Rietveld refinement is used to draw unit cell of synthesized Sn₂Pd single crystal using VESTA software, and the same is shown in inset of Fig. 1(b). A single unit cell

of Sn₂Pd is found to have 32 atoms of Sn and 16 atoms of Pd making the atomic formula to be Sn₃₂Pd₁₆. Single crystalline nature of synthesized Sn₂Pd single crystal is confirmed through FESEM image, which is shown in inset of Fig. 2(a). A typical slab like morphology can be seen in FESEM image, which shows that the synthesized sample is crystalline in nature. This slab like morphology signifies the layer-by-layer growth of the synthesized Sn₂Pd single crystal. Purity of the sample is verified through EDX measurement, which is shown in fig. 2(a). EDX spectra contains the peaks only for the constituent elements viz. Sn and Pd, which shows that no impurity of foreign atoms is present in the system. The composition of synthesized Sn₂Pd single crystal, obtained from EDX measurement is found to be Sn_{2.1}Pd. EDX mapping is also performed to check the distribution of constituent elements viz. Sn and Pd throughout the sample and is shown in fig. 2(b) and 2(c) respectively. Both the elements are found to be homogenously distributed throughout the sample. Homogenous distribution of Sn and Pd shows that none of the element remained in unreacted form in the synthesized sample, which is in agreement with the PXRD results. Both PXRD and EDX measurements shows that the synthesized Sn₂Pd single crystal is phase pure and no unreacted impurity is present in the sample.

Sn₂Pd has the general formula similar to materials Bi₂Pd, Sb₂Pd and Pb₂Pd, which all are superconducting in nature. Superconducting properties of Sn₂Pd have not been revealed yet, so transport measurements have been carried out on synthesized Sn₂Pd single crystal in a temperature range from 100K to 2K as shown in fig. 3(a). Sn₂Pd shows metallic behaviour as resistivity decreases with decrease in the temperature, and the same becomes almost constant at below 10K showing Fermi liquid behaviour. Resistivity data is fitted with the following formula

$$\rho(T) = \rho_0 + AT^2 \quad (1)$$

Here ρ_0 represents residual resistivity arising due to impurity scattering and is found to be 5.4m Ω -cm. The residual resistivity ratio (RRR) i.e., ρ_{100}/ρ_5 is found to be 1.06, which is rather low suggesting either the presence of structural disorder or low carrier concentration in the synthesized Sn₂Pd single crystal. The fitted plot is shown in the left inset of the fig. 3(a). Resistivity is well fitted with the applied formula up to 30K and starts to deviate above it, showing electron-electron (e-e) scattering to be the dominant scattering till 30K and electron-phonon (e-p) scattering dominating at higher temperatures. Interestingly, resistivity drops sharply below 2.8K, which can be attributed as a possible superconducting transition. At this

particular point resistivity is decreased almost 74%, but this transition does not reach to zero resistivity down to 2K (lowest temperature limit of instrument). A similar superconducting transition has also been observed in TaIrTe₄ [33], which is also a TSM. In TaIrTe₄ also, zero resistivity was not achieved, while resistivity was dropped almost 44% from the residual resistivity value. Here also, zero resistivity is not achieved but the resistivity is decreased significantly, hinting towards possible superconducting transition in synthesized Sn₂Pd single crystal. For the sake of repeatability, transport measurements were carried out on five different samples and all of them showed significant drop in resistivity, thus exhibiting the consistency of the occurrence of superconductivity. Sample S3, showed the maximum drop of around 74% as shown in fig. 3(a), and this sample is considered for other measurements. Further, the magneto transport (ρ -H) measurements have been carried out to check that the observed resistivity drop is a superconducting transition or not, as for a superconducting transition, upper critical field should be lowered as the temperature is increased. Fig. 3(b) shows ρ -H plot of synthesized Sn₂Pd single crystal, at 2K, 2.1K, 2.2K, 2.3K, 2.4K, 2.5K, 2.6K, 2.7K and 3K. Here also, zero resistivity is not observed below the critical field as observed in ρ -T plot in fig. 3(a). It is clear from fig. 3(b), that the sample is in superconducting state below 2.7K, as the resistivity is constant up to a certain magnetic field and the same is found to increase sharply when the field is increased further. This particular point, where resistivity jumps sharply is termed as critical field (H_c). Resistivity drop is not observed in ρ -H plot at 3K, showing the sample is clearly in normal state. H_c is shifted toward lower field value as the temperature is increased as can be seen in fig. 3(b), this is a typical behaviour of a conventional superconductor. The value of H_c at 2K is found to be around 270Oe. The observed transition in both ρ -T and ρ -H measurements cannot be attributed to the transition due to superconducting impurity of Sn, as the same is superconducting at 3.6K, which is much higher than the transition temperature observed in the present case. The presence of structural disorder can be the possible reason that zero resistivity is not achieved up to 2K and a larger transition width is observed. This is consistent with the observed low value of RRR. Presence of structural disorders in a superconducting sample leads to breaking of superconducting channels, due to which resistivity does not drop to zero value. In literature, non-occurrence of zero resistivity in a superconducting transition is attributed to possible quasi-1D superconductivity or surface superconductivity [33,34], in which only the helical surface states become superconducting. In quasi-1D superconductors, non-vanishing resistivity is observed in superconducting state due to phase slip events [35].

Fig. 4 shows AC magnetization measurements of synthesized Sn₂Pd single crystal at various AC fields viz. 30e, 50e, 70e, 90e, 110e and 130e. AC field frequency is set to 333Hz and the background DC field was set to 00e, throughout the measurement. The upper plot in fig. 3(b), is showing the imaginary part of AC magnetic moment (M'') while the lower plot is showing the real part (M') of the same. A superconducting transition is visible with T_c^{onset} at 2.8K, in both parts of AC magnetic moment. None of the moment saturates down to 2K, confirming superconducting volume fraction to be low, which is consistent with occurrence of non-zero resistivity in transport measurements. In both of the measurements, viz. transport and AC magnetization, the superconducting transition does not saturate, which shows that the observed superconducting transition is not the bulk property of the sample. At the same time, the observed diamagnetic signal in AC magnetization measurements opposes the possibilities of the superconducting transition to be termed as surface superconductivity. Heat capacity measurements are also carried out to check whether the observed superconductivity is bulk property of the sample or not. Fig. 5 shows the heat capacity measurements of synthesized Sn₂Pd single crystal, from 195K to 2K. Superconducting transition is not observed down to 2K, signifying the absence of bulk superconductivity in Sn₂Pd. Interestingly, although the observed Meissner effect in AC magnetization measurements suggest that the observed superconductivity is not due to the surface states, yet the observed low diamagnetic signal and non-occurrence of superconductivity in heat capacity measurements suggest that it is not the bulk superconductivity either. These results are similar to other superconducting topological material e.g. Pd doped Bi₂Te₃ [36-39]. Pd doped Bi₂Te₃ also shows low superconducting volume fraction and non-occurrence of zero resistivity, yet its superconductivity is not attributed to any superconducting impurities present in the sample [36]. Similarly, some other topological materials viz. Cu doped Bi₂Se₃ [36,40] and Ti doped NiTe₂ [41] shows finite resistivity and a low diamagnetic signal in the superconducting state. Here, Sn₂Pd also follows the same trend as the above-mentioned topological materials do, and the presence of structural disorders can be the possible reason for the observed properties. This warrants more experimental work to be performed on this system to further explore its structural and superconducting properties.

Further, specific heat data (C_p vs T) is utilized to determine the normal state parameters of synthesized Sn₂Pd single crystal. For this, low temperature C_p/T is plotted against T^2 as shown in inset of fig. 5. Heat capacity of a material is contributed by two terms viz. electronic

contribution to specific heat (C_{el}) and phonon contribution to specific heat (C_{ph}). Total specific heat is given by the following formula:

$$\frac{C_p}{T} = \gamma_n + \beta_n T^2 \quad (2)$$

here $\gamma_n T$ represents C_{el} and $\beta_n T^3$ represents C_{ph} . The coefficient associated with these terms are determined by fitting the C_p/T vs T^2 plot with linear equation as shown in inset of fig. 5. The intercept of linear fit provides the value of γ_n , which is known as Sommerfeld coefficient and the slope of the same provides the value of β_n , which is used in determining the value of Debye temperature (θ_D). The obtained values of γ_n and β_n are found to be $5.14 \pm 0.35 \text{ mJ mol}^{-1} \text{ K}^{-2}$ and $1.13 \pm 0.02 \text{ mJ mol}^{-1} \text{ K}^{-4}$. Sommerfeld coefficient is used to determine the Density of States at the Fermi level i.e., $D_c(E_F)$, which is given by the following formula,

$$\gamma_n = \frac{\pi^2 k_B^2 D_c(E_F)}{3} \quad (3)$$

The obtained value of $D_c(E_F)$ is found to be $2.19 \text{ states eV}^{-1} \text{ f.u.}^{-1}$. θ_D is related to β_n with the following formula

$$\theta_D = \left(\frac{12\pi^4 nR}{5\beta_n} \right)^{1/3} \quad (4)$$

Here $R=8.314 \text{ J mol}^{-1} \text{ K}^{-2}$ and n is the number of atoms in the formula unit, which is 3 for Sn_2Pd . The obtained value of θ_D for synthesized Sn_2Pd single crystal is 172.2K .

Normal state properties of Sn_2Pd are determined through magneto-transport measurements at temperatures above the critical temperature, and the same is shown in fig. 6(a). The variation in resistivity in a field range of $\pm 12\text{T}$, at various temperatures viz. 5K , 10K , 20K , 30K , 40K , 50K has been calculated in terms of MR% using the following formula:

$$MR\% = \left[\frac{\rho(H) - \rho(0)}{\rho(0)} \right] \times 100 \quad (5)$$

A significant MR% of around 50% has been observed at 5K , which gradually decreases with increasing the temperature. In normal metals, MR can arise due to change in trajectory of electrons on application of magnetic field, which has quadratic dependency on magnetic field. This behaviour is more pronounced at lower magnetic field. To check, whether the observed MR is normal one, which occurs in non-magnetic metallic systems, the low field MR% (upto 4T) has been plotted against H^2 , as shown in inset of fig. 6(a). It is clear from inset of fig. 6(a) that low field MR is not linear with H^2 , suggesting that the observed MR in Sn_2Pd is not normal

metallic MR. The reason for occurrence of MR in topological materials is different and is related to π Berry phase of TSS. The presence of π Berry phase results in destructive interference between two time-reversed paths of electrons. This destructive interference results in delocalization of electrons, which is known as WAL effect. Application of magnetic field disturbs the π Berry phase, and results in occurrence of positive MR in topological materials. The WAL induced MR shows cusp like behaviour at low magnetic field [42,43] as observed in present study on Sn₂Pd single crystal. In topological materials WAL arises due to the presence of topological surface state, while some materials with high spin orbit coupling also shows WAL effect [42-47].

The fitted ρ -T plot shows the presence of both e-e and e-p scattering processes, this information can be verified by applying Kohler scaling laws in MR data. Kohler's rule suggests that MR% should be a function of $H\tau$, where τ is the time spent in scattering events of conduction electrons. τ is inversely proportional to zero field resistivity $\rho(0)$, so MR% should be a function of H/ρ_0 . If a system preserves the Kohler's law, there exists only a single e-e scattering and MR% vs H/ρ_0 plots at different temperatures should collapse into each other [48-50]. To check this, MR% is plotted against H/ρ_0 and plotted in fig. 6(c). It is clear from fig. 6(c), that Kohler rule is violated in Sn₂Pd single crystal as all the MR% vs H/ρ_0 plots at different temperatures do not merge into a single curve. This violation of Kohler's law suggests that two scattering processes viz. e-e and e-p scattering are present in the synthesized Sn₂Pd single crystal. This is further verified by calculation of phase coherence length l_ϕ at different temperatures.

Fig. 6(c) shows the low field (± 0.6 T) MC data of synthesized Sn₂Pd single crystal at various temperatures viz. 5K, 10K, 20K, 30K, 40K & 50K. The low field MC data is fitted with HLN equation [51], which is as follows

$$\Delta\sigma(H) = -\frac{\alpha e^2}{\pi h} \left[\ln\left(\frac{B_\phi}{H}\right) - \Psi\left(\frac{1}{2} + \frac{B_\phi}{H}\right) \right] \quad (6)$$

Here $\Delta\sigma(H)$ symbolizes $[\sigma(H)-\sigma(0)]$, B_ϕ is termed as characteristic field, which is given by $B_\phi = \frac{h}{8e\pi l_\phi^2}$, Ψ is digamma function. l_ϕ denotes the phase coherence length, which is the maximum length, which is travelled by the electron while maintaining its phase. Another important parameter, which is obtained from HLN fitting is the pre-factor α . The value of α confirms that whether the WAL effect is present in the system or not, as a negative value of α

signifies the presence of WAL effect, while a positive value of the same shows the presence of weak localization (WL) effect. The value of α , gives the information about the conduction mechanism, whether the conduction is solely dominated by surface states or the bulk states also contribute in conduction mechanism. α is supposed to take value -0.5 for single TSS [42], while for two independent TSS the value of α should be equal to -1. The deviation of α from -0.5 and -1, signifies that the TSS are connected through bulk states [52-54], and the bulk states also contribute to conduction mechanism. HLN fitted low field (± 0.6 T) MC data at 5K, 10K, 20K, 30K, 40K and 50K is shown by solid black line in Fig. 6(c). The value of pre-factor α at 5K is found to be -0.56, the negative value of α confirms the presence of WAL effect in synthesized Sn₂Pd single crystal. The obtained value of α is close to -0.5 suggesting that single conducting channel is present in the system, while its deviation from standard value of -0.5, suggests that the bulk states also contribute in the conduction mechanism. The value of α tends to decrease monotonically as the temperature is increased, as shown in fig. 6(d). The value of α is very close to standard value -0.5 at 5K and 10K, suggesting that surface states dominate in conduction mechanism at both of these temperatures. Further, at higher temperatures viz. 20K, 30K, 40K and 50K, the value of α is deviated largely from -0.5 significantly, suggesting that the conduction phenomenon is mainly governed by the bulk states at these temperatures. Phase coherence length l_ϕ , is also calculated through HLN modelling, and the variation in l_ϕ^{-2} with respect to temperature is shown in fig. 6(d) by blue symbols. The variation of l_ϕ with respect to temperature gives important information about the dephasing mechanism and scattering processes. The Nyquist criterion suggests that only a single scattering process i.e. electron-electron (e-e) scattering is included in dephasing mechanism if l_ϕ^{-2} varies linearly with temperature [55,56]. A deviation of l_ϕ^{-2} vs T plot from linearity suggests that there exists another scattering process, which is electron-phonon (e-p) scattering. It is clear from fig. 6(d), that the variation in l_ϕ^{-2} is not linear with respect to temperature, suggesting the contribution of both e-e and e-p scattering process in dephasing mechanism in Sn₂Pd single crystal. The involvement of both the scattering processes is in accordance with the violation of Kohler rule in MR vs H/ρ_0 plot. Further, the l_ϕ^{-2} vs T plot is fitted with the following power law [57] shown by solid black line in fig. 6(d):

$$\frac{1}{l_\phi^2(T)} = \frac{1}{l_\phi^2(0)} + A_{e-e}T^p + A_{e-p}T^q \quad (7)$$

Here $l_{\phi}(0)$ represents the dephasing length at absolute zero and the contribution from e-e and e-p scattering are shown by $A_{e-e}T^p$ and $A_{e-p}T^q$ respectively. The value of p and q from fitting are found to be 1 and 2 respectively, which shows the 2-D nature of observed WAL effect, which is observed in other topological materials [54,58]. The obtained value of $l_{\phi}(0)$ from power law fitting is 102nm, and the values of A_{e-e} and A_{e-p} are found to be 2.185×10^{-6} and 3.32×10^{-8} . The values of pre factor α and dephasing length and phase coherence length l_{ϕ} at various temperatures obtained from HLN fitting are listed in table-2.

Conclusion:

Summarily, this article reports a detailed report on synthesis and magneto transport measurements of an unexplored topological material, Sn_2Pd . Phase purity of stoichiometry is evidenced through XRD and EDX measurements. Sn_2Pd is found to show evidences of possible superconducting transition in the form of significant resistivity drop in both ρ -T and ρ -H measurements, while zero resistivity is not achieved. Superconducting transition is not observed in heat capacity measurements, which further shows the absence of bulk superconducting properties. A non-saturating LMR is observed in magneto transport measurements, showing the possible presence of TSS, which is further confirmed by HLN fitting of low field MC data. This is *the first report on magneto transport measurements* showing the experimental evidence of topological properties along with the low temperature (below 2.8K) surface superconductivity in Sn_2Pd single crystal.

Acknowledgment:

Authors would like to thank Director of National Physical Laboratory, New Delhi for his keen interest. M. M. Sharma would like to thank CSIR, India for research fellowship and AcSIR, Ghaziabad for Ph.D. registration.

Table-1

Parameters obtained from Rietveld refinement:

Cell Parameters	Refinement Parameters
Cell type: Tetragonal	$\chi^2=2.20$
Space Group: I 41/acd	$R_p=7.37$
Lattice parameters: $a=b=6.492(4)\text{\AA}$	$R_{wp}=9.66$
& $c=24.362(2)\text{\AA}$	$R_{exp}=6.51$
$\alpha=\beta=\gamma=90^\circ$	

Cell volume: 1026.959Å ³	
Density: 8.894 g/cm ³	
Atomic co-ordinates:	
Sn1 (0.15785,0.40785,0.125)	
Pd (0,0.25,0.31665)	
Sn2 (0.24741,0,0.25)	

Table: 2

Low field (up to 1 Tesla) HLN fitted parameters of Sn₄Au single crystal

Temperature(K)	α	$l\phi(\text{nm})$
5	-0.5608	95.06
10	-0.4749	91.8619
20	-0.2694	83.7321
30	-0.2335	72.0596
40	-0.2319	63.9714
50	-0.1986	59.5581

Figures Caption:

Fig. 1(a): Schematic of heat treatment used to synthesize Sn₂Pd single crystal.

Fig. 1(b): Rietveld refined PXRD pattern of synthesized Sn₂Pd single crystal in which the red symbols are showing the experimental data and the solid black line is showing the Rietveld refined data, the inset is showing the unit cell of the same drawn by using VESTA software where blue circles are showing the Pd atoms and the orange circles are showing the Sn atoms.

Fig. 2(a): EDX spectra showing the peaks of constituent elements of Sn₂Pd single crystal in which inset is showing the FESEM image of the same. **(b)** EDX mapping of Sn atoms **(c)** EDX mapping of Pd atoms.

Fig. 3(a): ρ vs T plot of synthesized Sn₂Pd single crystal in temperature range from 100K to 2K, in which right inset is showing the zoomed view of ρ vs T plot in proximity of superconducting transition and the left inset is showing the fitted ρ vs T plot in normal state of Sn₂Pd from 5K to 100K.

Fig. 3(b): ρ vs H plot of synthesized Sn₂Pd single crystal at temperatures 2K, 2.1K, 2.2K, 2.3K, 2.4K, 2.5K, 2.6K, 2.7K and 3K.

Fig. 4: AC magnetization measurements of Sn₂Pd single crystal at various AC fields viz. 30e, 50e, 70e, 90e, 110e & 130e.

Fig. 5: C_p vs T plot of synthesized Sn₂Pd single crystal, in which inset is showing the fitted C_p/T vs T² plot of the same.

Fig. 6(a): MR% vs H plot in a field range of ±12T at various temperatures viz. 5K, 10K, 20K, 30K, 40K and 50K, in which inset is showing the variation in MR% with respect to square of applied field upto 4T.

Fig. 6(b): MR% vs H/ρ₀ plots for Kohler's scaling of MR at various temperatures viz. 5K, 10K, 20K, 30K, 40K and 50K.

Fig. 6(c): HLN fitted low field (±12T) MC data of Sn₂Pd single crystal at 5K, 10K, 20K, 30K, 40K and 50K, in which the HLN fitted plots are shown by solid black lines.

Fig. 6(d): Variation in parameters obtained from HLN fitting with respect to temperature in which red symbols are showing the variation in pre factor α with respect to temperature and the blue symbols are showing the same for inverse of square of phase coherence length (l_φ⁻²). The solid black line is showing the power law fitted l_φ⁻² vs T plot of synthesized Sn₂Od single crystal

References:

1. Xiao-Liang Qi and Shou-Cheng Zhang, Rev. Mod. Phys. **83**, 1057 (2011).
2. A. A. Burkov, Nature Mater **15**, 1145 (2016).
3. Masatoshi Sato and Yoichi Ando, Rep. Prog. Phys. **80**, 076501 (2017).
4. Hao Zheng and Jin-Feng Jia, Chinese Phys. B **28**, 067403 (2019).
5. Mingyang Chen, Xiaoyu Chen, Huan Yang, Zengyi Du and Hai-Hu Wen Science **4**, 1084 (2018).
6. V. Mourik, K. Zuo, S. M. Frolov, S. R. Plissard, E. P. A. M. Bakkers, and L. P. Kouwenhoven, Science **336**, 1003 (2012).
7. Y. S. Hor, A. J. Williams, J. G. Checkelsky, P. Roushan, J. Seo, Q. Xu, H. W. Zandbergen, A. Yazdani, N. P. Ong, and R. J. Cava, Phys. Rev. Lett. **104**, 057001 (2010).
8. Yunsheng Qiu, Kyle Nocona Sanders, Jixia Dai, Julia E. Medvedeva, Weida Wu, Pouyan Ghaemi, Thomas Vojta, Yew San Hor, arXiv:1512.03519 (2015).
9. Zhongheng Liu, Xiong Yao, Jifeng Shao, Ming Zu, Li Pi, Shun Tan, Changjin Zhang, Yuheng Zhang, J. Am. Chem. Soc. **137**, 10512 (2015).
10. Y.S.Hor, J.G.Checkelsky, D.Qu, N.P.Ong, R.J.Cava, J. Phys. Chem. Solids **72**, 572 (2011).
11. Zhiwei Wang, A. A. Taskin, Tobias Frölich, Markus Braden, and Yoichi Ando, Chem. Mater. **28**, 779 (2016).

12. Jian Wang, *Nat. Sci. Rev.* **6**, 199 (2019).
13. Yanfei Zhao, Haiwen Liu, Chenglong Zhang, Huichao Wang, Junfeng Wang, Ziquan Lin, Ying Xing, Hong Lu, Jun Liu, Yong Wang, Scott M. Brombosz, Zhili Xiao, Shuang Jia, X. C. Xie, and Jian Wang, *Phys. Rev. X* **5**, 031037 (2015).
14. Tiantian Zhang, Yi Jiang, Zhida Song, He Huang, Yuqing He, Zhong Fang, Hongming Weng & Chen Fang, *Nature* **566**, 475 (2019).
15. Heng Gao, Jörn W.F. Venderbos, Youngkuk Kim, and Andrew M. Rappe, *Annual Review of Materials Research* **49**, 153 (2019).
16. Jie Yang, Zhi-Yong Song, Lei Guo, Heng Gao, Zhuo Dong, Qiang Yu, Ren-Kui Zheng, Ting-Ting Kang, and Kai Zhang, *Nano Lett.* **21**, 10139 (2021).
17. Mario Novak, Satoshi Sasaki, Kouji Segawa, and Yoichi Ando, *Phys. Rev. B* **91**, 041203(R) (2015).
18. Ian A. Leahy, Yu-Ping Lin, Peter E. Siegfried, Andrew C. Treglia, Justin C. W. Song, Rahul M. Nandkishore, and Minhyea Lee, *PNAS* **115**, 10570 (2018).
19. M. Sakano, K. Okawa, M. Kanou, H. Sanjo, Okuda, Sasagawa & K Ishizaka, *Nat. Comm.* **6**, 8595 (2015).
20. B T Wang and Elena R Margine, *J. Phys.: Condens. Matter* **29**, 325501 (2017).
21. Ayo Kolapo, Tingxin Li, Pavan Hosur & John H. Miller Jr., *Sci Rep* **9**, 12504 (2019).
22. B. T. Matthias, T. H. Geballe, and V. B. Compton, *Rev. Mod. Phys.* **35**, 1 (1963).
23. Ramakanta Chapai, Yating Jia, W. A. Shelton, Roshan Nepal, Mohammad Saghayezhian, J. F. DiTusa, E. W. Plummer, Changqing Jin, and Rongying Jin, *Phys. Rev. B* **99**, 161110(R) (2019).
24. Nitesh Kumar, Mengyu Yao, Jayita Nayak, Maia G. Vergniory, Jörn Bannies, Zhijun Wang, Niels B. M. Schröter, Vladimir N. Strocov, Lukas Mühler, Wujun Shi, Emile D. L. Rienks, J. L. Mañes, Chandra Shekhar, Stuart S. P. Parkin, Jörg Fink, Gerhard H. Fecher, Yan Sun, B. Andrei Bernevig, and Claudia Felser, *Adv. Mater.* **32**, 1906046 (2020).
25. Z. P. Sun, C. Q. Hua, X. L. Liu, Z. T. Liu, M. Ye, S. Qiao, Z. H. Liu, J. S. Liu, Y. F. Guo, Y. H. Lu, and D. W. Shen, *Phys. Rev. B* **101**, 155114 (2020).
26. Xiàn Yáng, Tyler A. Cochran, Ramakanta Chapai, Damien Tristant, Jia-Xin Yin, Ilya Belopolski, Zǐjiā Chéng, Daniel Multer, Songtian S. Zhang, Nana Shumiya, Maksim Litskevich, Yuxiao Jiang, Guoqing Chang, Qi Zhang, Ilya Vekhter, William A. Shelton, Rongying Jin, Su-Yang Xu, and M. Zahid Hasan, *Phys. Rev. B* **101**, 201105(R) (2020).
27. Arushi, K. Motla, A. Kataria, S. Sharma, J. Beare, M. Pula, M. Nugent, G. M. Luke, and R. P. Singh, *Phys. Rev. B* **103**, 184506 (2021).
28. M. M. Sharma, N.K. Karn, Poonam Rani, R.N. Bhowmik, V.P.S. Awana, **arXiv:2112.07276** (2021).
29. J. R. Chamorro, P. Chauhan, C. Sun, N. Varnava, M. J. Winiarski, N. Ng, H. K. Vivanco, L. A. Pressley, C. M. Pasco, D. Vanderbilt, Yi Li, N. P. Armitage, T. M. McQueen, **arXiv:2112.10840** (2021).
30. X. -H. Tu, P. -F. Liu, W. Yin, J. -R. Zhang, P. Zhang, B. T. Wang, *Mater. Today Phys.* **24**, 100674 (2022).
31. Peng-Fei Liu, Jingyu Li, Xin-Hai Tu, Huabing Yin, Baisheng Sa, Junrong Zhang, David J. Singh, and Bao-Tian Wang, *Phys. Rev. B* **102**, 155406 (2020).
32. Bernd Kunnen, Dirk Niepmann, Wolfgang Jeitschko, *J. Alloys & Comp.* **309**, 1 (2000).

33. Ying Xing, Zhibin Shao, Jun Ge, Jiawei Luo, Jinhua Wang, Zengwei Zhu, Jun Liu, Yong Wang, Zhiying Zhao, Jiaqiang Yan, David Mandrus, Binghai Yan, Xiong-Jun Liu, Minghu Pan, Jian Wang, *Nat. Sci. Rev.* **7**, 579 (2020).
34. Mingliang Tian, Jian Wang, Wei Ning, Thomas E. Mallouk, and Moses H. W. Chan, *Nano Lett.* **15**, 1487 (2015).
35. Bertrand I. Halperin, Gil Refael and Eugene Demler, *International Journal of Modern Physics B* **24**, 4039 (2010).
36. Y.S. Hor, J.G. Checkelsky, D. Qu, N.P. Ong, R.J. Cava, *J. Phys. Chem. Sol.* **72**, 572 (2011).
37. Amit, Y. Singh, *J. Supercond. Nov. Magn.* **29**, 1975 (2016).
38. M. M. Sharma, Lina Sang, Poonam Rani, X. L. Wang & V. P. S. Awana, *J. Supercond. Nov. Magn.* **33**, 1243–1247 (2020).
39. Xianyu Wang, Fei Jiao, Qingyin Tian, Shu Zhu, Xiangqing Dong, Jianping Sun, Lingbo Cai, Jiayuan Hu, Chenhang Xu, Qing Lu, Shugang Tan, Cao Wang, Qiang Jing, Bo Liu & Dong Qian, *J. Supercond. Nov. Magn.* **34**, 3045 (2021).
40. Satoshi Sasaki, M. Kriener, Kouji Segawa, Keiji Yada, Yukio Tanaka, Masatoshi Sato, and Yoichi Ando, *Phys. Rev. Lett.* **107**, 217001 (2011).
41. B.S. de Lima, R.R. de Cassia, F.B. Santos, L.E. Correa, T.W. Grant, A.L.R. Manesco, G.W. Martins, L.T.F. Eleno, M.S. Torikachvili, A.J.S. Machado, *Solid State Commun.* **283**, 27 (2018).
42. K. Shrestha, D. Graf, V. Marinova, B. Lorenz, and C. W. Chu, *J. App. Phys.* **122**, 145901 (2017).
43. W. Wang, W. Q. Zou, L. He, J. Peng, R. Zhang, X. S. Wu, and F. M. Zhang, *J. Phys. D: Appl. Phys.* **48**, 205305 (2015).
44. Bin Xia, Peng Ren, Azat Sulaev, Peng Liu, Shun-Qing Shen, and Lan Wang, *Phys. Rev. B* **87**, 085442 (2013).
45. Zhipeng Hou, Yue Wang, Guizhou Xu, Xiaoming Zhang, Enke Liu, Wenquan Wang, Zhongyuan Liu, Xuekui Xi, Wenhong Wang, Guangheng Wu, *Appl. Phys. Lett.* **106**, 102102 (2015).
46. Guizhou Xu, Wenhong Wang, Xiaoming Zhang, Yin Du, Enke Liu, Shouguo Wang, Guangheng Wu, Zhongyuan Liu, and Xi Xiang Zhang, *Sci. Rep.* **4**, 5709 (2014).
47. Zhipeng Hou, Yue Wang, Enke Liu, Hongwei Zhang, Wenhong Wang, and Guangheng Wu, *Appl. Phys. Lett.* **107**, 202103 (2015).
48. J. M. Ziman, *Electrons and Phonons* (Oxford University Press, 1960).
49. Ye-Cheng Luo, Yang-Yang Lv, Rui-Ming Zhang, Lu Xu, Zhi-An Zhu, Shu-Hua Yao, Jian Zhou, Xiao-Xiang Xi, Y. B. Chen, and Yan-Feng Chen, *Phys. Rev. B* **103**, 064103 (2021).
50. A. Malinowski, V. L. Bezusyy, and P. Nowicki, *Phys. Rev. B* **95**, 014521 (2017).
51. S. Hikami, A. I. Larkin, and Y. Nagaoka, *Prog. of Theo. Phys.* **63**, 707 (1980).
52. J. Chen, H. J. Qin, F. Yang, J. Liu, T. Guan, F. M. Qu, G. H. Zhang, J. R. Shi, X. C. Xie, C. L. Yang, K. H. Wu, Y. Q. Li, and L. Lu, *Phys. Rev. Lett.* **105**, 176602 (2010).
53. Hui Li, Huan-Wen Wang, Yang Li, Huachen Zhang, Shuai Zhang, Xing-Chen Pan, Bin Jia, Fengqi Song, and Jiannong Wang, *Nano Lett.* **19**, 2450 (2019).
54. Priyanath Mal, Bipul Das, G. Bera, G. R. Turpu, C. V. Tomy & Pradip Das, *J Mater Sci: Mater Electron* **33**, 1 (2022).
55. J J Lin and J P Bird, *J. Phys.: Condens. Matter* **14**, R501 (2002).

56. Namrata Bansal, Yong Seung Kim, Matthew Brahlek, Eliav Edrey, and Seongshik Oh, Phys. Rev. Lett. **109**, 116804 (2012).
57. Saurav Islam, Semonti Bhattacharyya, Hariharan Nhalil, Mitali Banerjee, Anthony Richardella, Abhinav Kandala, Diptiman Sen, Nitin Samarth, Suja Elizabeth, and Arindam Ghosh, Phys. Rev. B **99**, 245407 (2019).
58. Wen Jie Wang, Kuang Hong Gao & Zhi Qing Li, Sci Rep **6**, 25291 (2016).

Fig. 1(a)

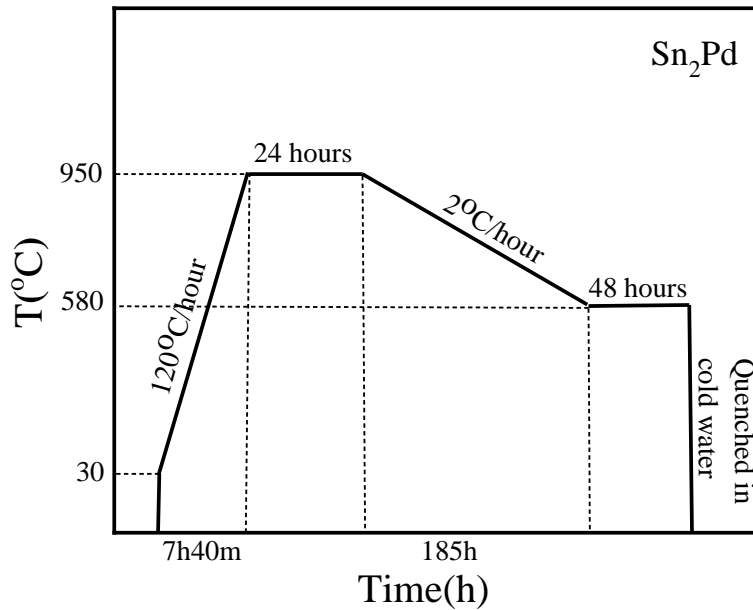


Fig. 1(b)

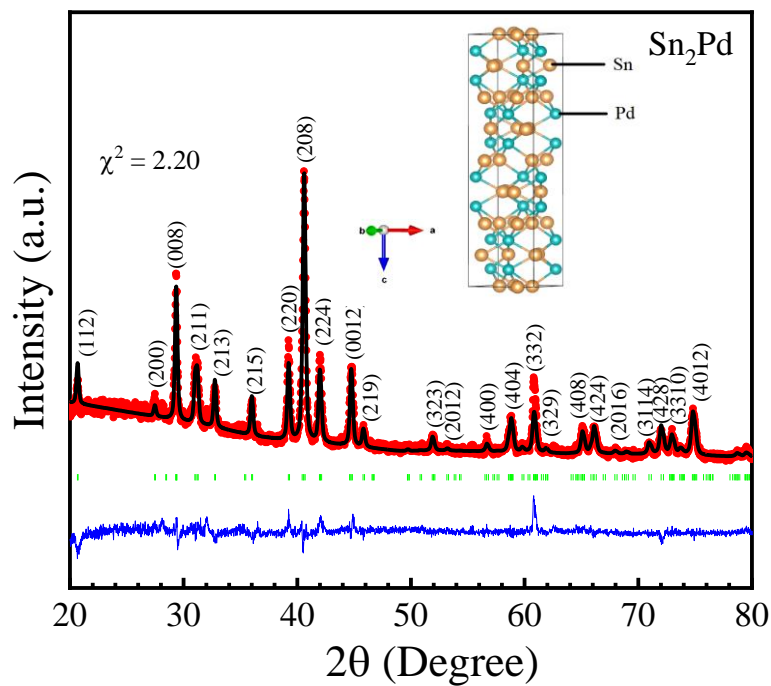


Fig. 2(a)

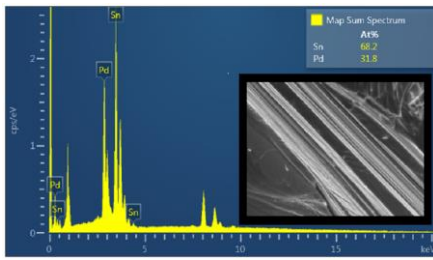


Fig. 2(b)

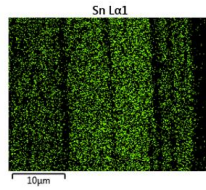


Fig. 2(c)

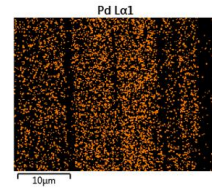


Fig. 3(a)

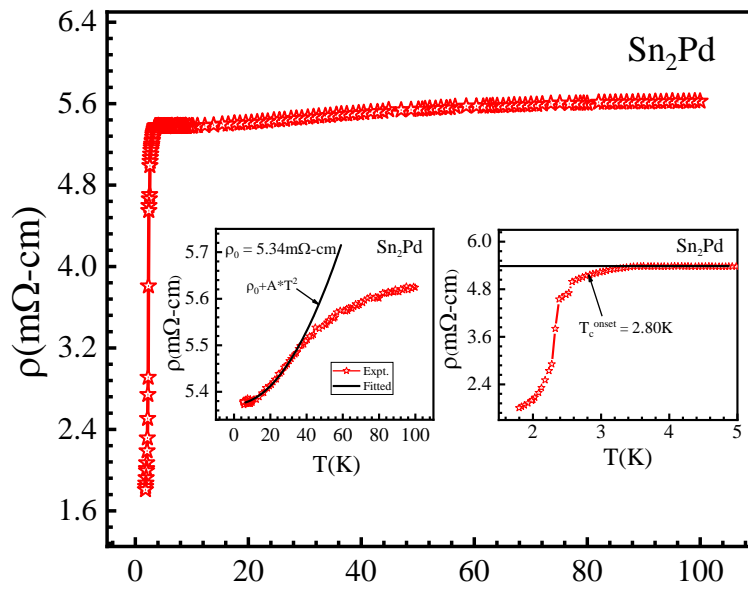


Fig. 3(b)

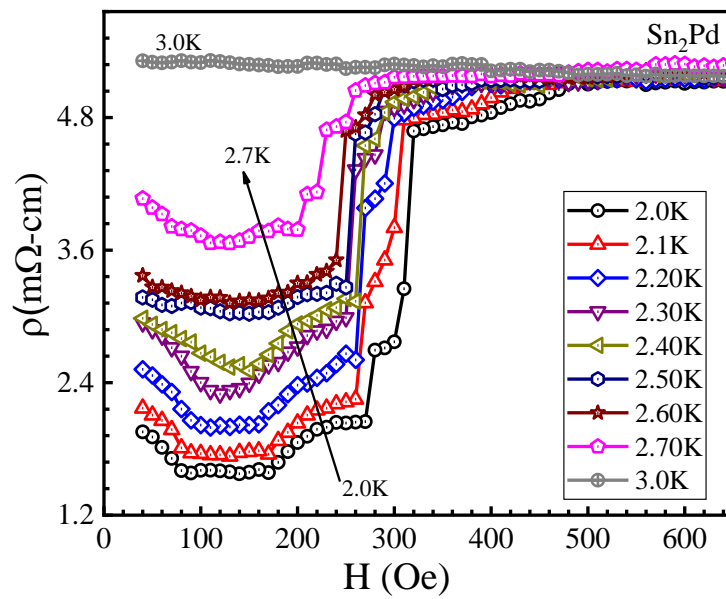


Fig. 4

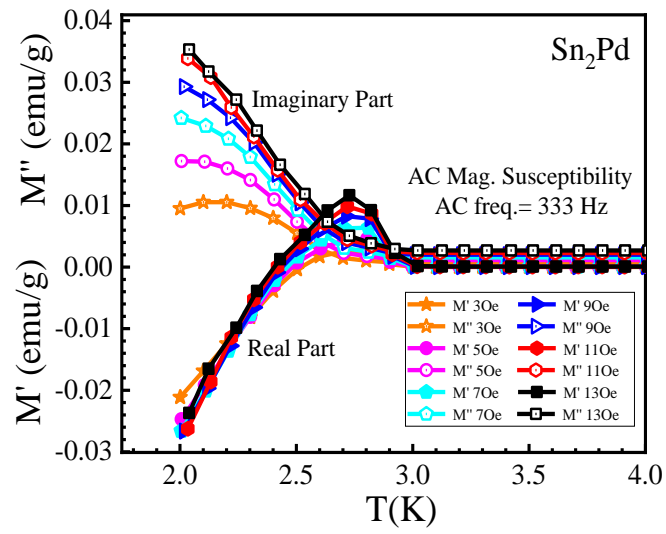


Fig. 5

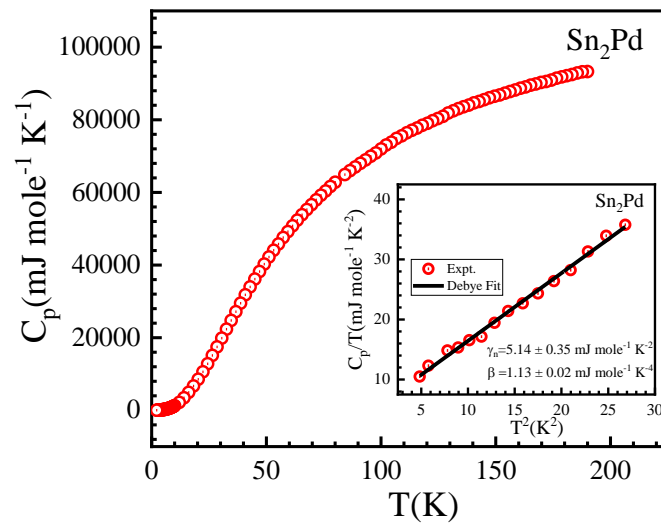


Fig. 6(a)

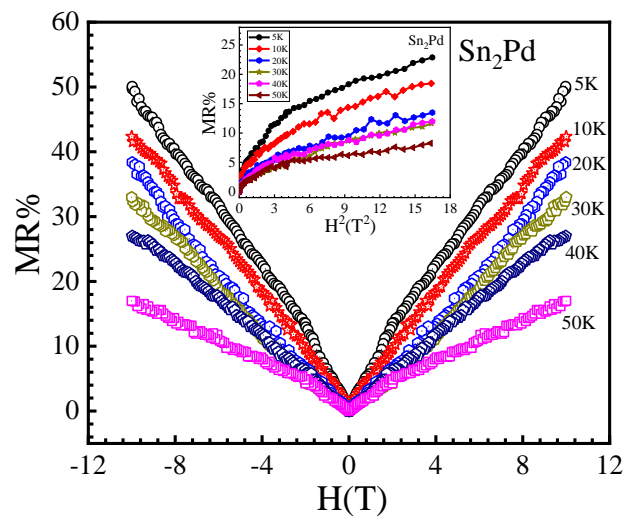


Fig. 6(b)

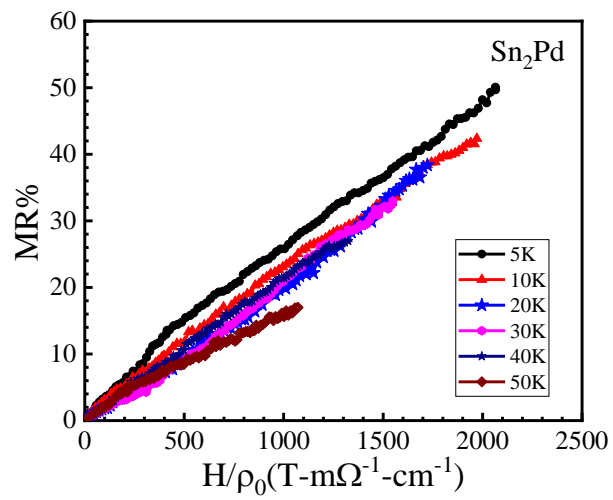


Fig. 6(c)

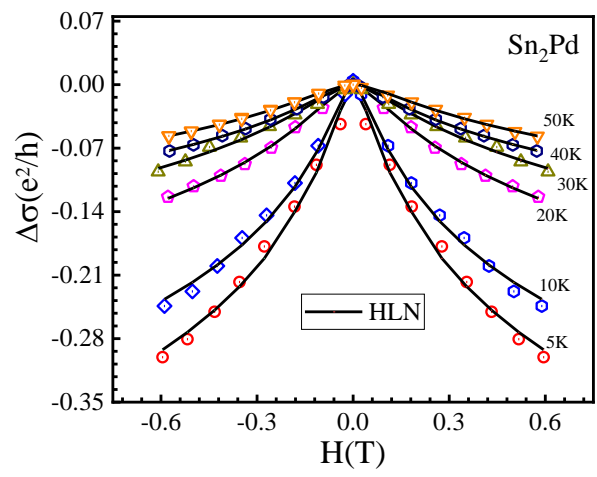


Fig. 6(d)

